Neuronal cascades shape whole-brain functional dynamics at rest

Giovanni Rabuffo*, Jan Fousek, Christophe Bernard, Viktor Jirsa

Institut de Neurosciences des Systèmes, Aix-Marseille University, Marseille, France

December 26, 2020

Abstract

At rest, mammalian brains display a rich complex spatiotemporal behavior, which is reminiscent of healthy brain function and has provided nuanced understandings of several major neurological conditions. Despite the increasingly detailed phenomenological documentation of the brain's resting state, its principle underlying causes remain unknown. To establish causality, we link structurally defined features of a brain network model to neural activation patterns and their variability. For the mouse, we use a detailed connectome-based model and simulate the resting state dynamics for neural sources and whole brain imaging signals (Blood-Oxygen-Level-Dependent (BOLD) , Electroencephalography (EEG)). Under conditions of near-criticality, characteristic neuronal cascades form spontaneously and propagate through the network. The largest neuronal cascades produce short-lived but robust co-fluctuations at pairs of regions across the brain. During these co-activation episodes, long-lasting functional networks emerge giving rise to epochs of stable resting state networks correlated in time. Sets of neural cascades are typical for a resting state network, but different across. We experimentally confirm the existence and stability of functional connectivity epochs comprising BOLD co-activation bursts in mice (N=19). We further demonstrate the leading role of the neuronal cascades in a simultaneous EEG/fMRI data set in humans (N=15), explaining a large part of the variability of functional connectivity dynamics. We conclude that short-lived neuronal cascades are a major robust dynamic component contributing to the organization of the slowly evolving spontaneous fluctuations in brain dynamics at rest.

*Corresponding author giovanni.rabuffo@univ-amu.fr

1 Introduction

Functional Magnetic Resonance Imaging (fMRI) reveals that blood-oxygenation-level-dependent (BOLD) activity is highly correlated between brain regions; an observation consistent across several mammalian species. Network theoretical approaches reduce the complexity of the brain's activation patterns to a simple representation in terms of a network's nodes, the brain regions, and edges, the pair-wise interactions. In the traditional node-centric perspective, Functional Connectivity (FC) measures brain network interactions and provides a useful metric to characterize the organization of brain activity during diverse cognitive states [1, 2, 3, 4], aging [5, 6, 7], behavior [8, 9] and pathologies [10, 11, 12, 13, 14]. At rest, characteristic networks, the resting-state networks ($RSNs$), have been systematically observed in human [15, 16] and non-human [17] primates, but also in rats [18, 19] and mice [20, 21, 22, 23]. $RSNs$ have been associated with spanning the subspace in which a majority of the spontaneous resting state fluctuations evolve. Accordingly, FC patterns are not static, but evolve in time, alternating epochs of relative stability of FC, followed by rapid re-organization to another longer lasting epoch of invariant FC [24, 25, 26, 27, 28, 29, 30]. The temporal organization of FC patterns introduces an edge-centric perspective into network science, which allows to define the dynamic Functional Connectivity (dFC) [31, 32]. dFC reduces the complexity of the brain signals to the slow evolution of FC, with rich applications in brain health, aging and disease [33, 34, 35, 36, 37, 38]. A related spatial metric is the edge functional connectivity (eFC) [39], which estimates the edge communities structure directly from the edge times series. Despite the increasingly detailed phenomenological documentation of the brain's resting state, its principle underlying causes remain unknown. To establish causality, we here systematically investigate co-activation (CA) events between pairs of brain nodes within a biologically realistic large-scale network model and derive in-silico-inspired strategies to shed light on the relationship of neuronal dynamics, FC and dFC. The hypotheses developed in-silico found in-vivo confirmations on various species, mouse and man, across fMRI and EEG imaging modalities. Our here advocated approach emphasizes the coordination of research workflows across-domains and demonstrates how model-driven research leads to discovery of novel biomarkers.

To close the gap between neuronal sources and brain imaging signals, we use The Virtual Brain (TVB) simulation platform [40]. TVB is a network simulator, specialized for the use of white-matter connectomes of multiple species including human [41] and mouse brains [42]. As networks are defined on large scales, TVB considers time delays due to finite signal transmission speeds and a range of source-sensor maps between network nodes and sensor locations of brain imaging modalities including BOLD fMRI, EEG and MEG. A variety of mean field models of neuronal activity are readily available in TVB. Previous TVB modeling studies of the resting state have typically used highly simplified network node models, justified by their use limited to a single imaging modality. Derivatives of the Wong Wang model [43] are used for applications of the BOLD signal [44, 32, 45]; and oscillator models such as Stefanescu-Jirsa [46], Jansen-Rit [47] or Kuramoto [48] models for EEG and MEG signals. None of these efforts attempted multi-modality modeling and validation, except in a hybrid approach [49], which used the empirical EEG source signal to drive and explain the modelled fMRI signal. For a mechanistic multi-scale explanation and cross-modal multi-species validation, we adapt a novel neural mass model (NMM), which has been previously derived as the exact thermodynamic limit of an infinite number of coupled quadratic integrate-and-fire neurons [50]. This analytic step allows to derive the average firing rate and membrane potential of a mesoscopic neuronal population, thus providing suitable neural mass variable while keeping track of the internal organization of the constituent neurons. Importantly, we here demonstrate that the mathematical structure of the novel NMM combines faithfully the dynamic properties of the previously used connectome-based models in

both imaging modalities. We use this approach for systematic exploration and parameter sweeps of the dynamic repertoire of the model across imaging modalities and then demonstrate that neuronal cascades accompanied by a bursty BOLD-CA dynamics spontaneously emerge in the model, in conjunction with a non-trivial dFC. The largest neuronal cascades give rise to the bursts of BOLD-CA events, which in turn evoke stable long-lasting FC states. Theoretical predictions are verified experimentally in mice and humans. We propose that the largest neuronal cascades play a central role in shaping whole brain dynamics at rest.

2 Results

The simulated whole-brain dynamics is obtained by the numerical integration of the local neural mass model equations coupled over a detailed mouse connectome [42]. The brain structure (Figure 1A) is imported from the tracer experiments of the Allen Institute and it is parceled into anatomic regions of interest, associated with the network nodes [51].

Once a working regime is chosen by the selection of global and local model parameters, the raw outcome of the simulation consists of a high time-resolution neuroelectric signal. Namely, the average firing rate r and membrane potential V for each brain region. In what follows, we will also refer to the average firing rate activity as the simulated EEG data. With a further processing step, we obtain a low time-resolution simulated BOLD activity by filtering the membrane potentials through the Balloon-Windkessel model [52] (Figure 1B).

Varying the model parameters we can simulate different network configurations. As a first step, we want to qualitatively reproduce the whole-brain dFC patterns of activity which are typically observed in empiric BOLD signals. We analyze the situation in which the local model parameters are fixed everywhere such that any decoupled region is in a bi-stable configuration (see Methods). The model is coupled over the Allen mouse connectome and the communication across the brain regions is mediated by the average firing rate of the sender regions, which act as excitatory currents altering the average membrane potential of the receiving regions (see Methods).

There exists several dFC measures which describe the dynamic evolution of the functional brain patterns [31, 53, 54, 55, 56, 57]. The most diffuse, is based on a sliding window approach [25]. In brief, inside each time window, a static FC is computed as the correlation matrix of the BOLD activities. Then, the entries of the windowed-dFC (dFC_w) matrix are defined as the correlation between the FCs at different windows (see Methods and Figure S1A, top panel). For our analysis, we mainly exploit dynamic functional measures derived in an edge-centric approach, where the edge dynamics is defined by the product of the z-scored BOLD activity at each couple of nodes [39]. The resulting co-activation (CA) time series (Figure 1C) are associated to each network edge and have the same time resolution of the BOLD signals. At a given frame, a high co-activation amplitude corresponds to the simultaneous fluctuation of the nodes at the edge borders away from their respective baselines. Therefore, it is important to keep in mind that this measure can be affected by random noisy fluctuations. Also, in order to avoid biasing following the z-score preprocessing one must ensure that the mean and standard deviation of the BOLD time series are temporally invariant across several events [58]. Holding on to these recommendations, one can interpret the CA time series of an edge as the temporal unfolding of the correlation between the signals at the extremal nodes, since its time average defines their Pearson Correlation Coefficient. Each column in Figure 1C (top) represents an instantaneous realization of the Functional Connectivity (iFC) at a time t. The static FC is obtained by averaging over all iFC in the time domain. The edge dynamic functional connectivity (dFC_e) is defined (without the use of sliding windows) by the Pearson Correlation of the iFCs at each couple of times t_i and t_j.

2.1 Multiple pathways towards a dynamic functional organization

The synthetic whole-brain dynamics is tested by tuning two global parameters: the global coupling G representing the impact of the structure over the local dynamics, and the intensity N of the stochastic currents entering at each time step in every region, which simulate the effect of a generic environmental noise (thermodynamic, chemical, synaptic,...). We systematically explored the parameter space spanned by (G, N) and simulated several minutes of neuroelectric

and BOLD activity for each parametrization. Then, we looked for regions of the parameter space where the dFC matrices show off-diagonal block structures. As a measure of non-triviality, we defined the 'switching index' i.e., the variance of the upper triangular part of the dFC_w matrix (Figure 2). Notice that, in general, to a non-trivial dFC_w corresponds a dFC_e with high off-diagonal values, reporting a high correlation between iFCs at different times. In the Methods section we compare the edge-based and the windowed dFC measures.

We show the presence of two configurations of the global parameters in which the simulated microscopic activity gives rise to a large-scale functional dynamics (Figure 2). The two regimes identify distinct pathways towards a dynamic functional organization, where the respective neuroelectric correlates are qualitatively different.

- In the first case, a weak structural coupling is insufficient to promote any region into a highly firing rate state. However, all the regions can potentially reach such state for a short transient thanks to a strong stochastic drive. Therefore we refer to this as the *monostable* regime (Figure 2, bottom left).
- In the other scenario, the stronger structural coupling pushes a subset of regions into a strongly active state leaving the remaining regions in the down state. A weak stochastic drive ensures a stable dynamics with few regions jumping between the up and down states. We call this the *bistable* regime (Figure 2, bottom right).

In this article we focus on the (G, N) values corresponding to the red boxes in Figure 2, top. Summarizing, the balance between the local dynamics and the global connectivity, together with appropriate levels of perturbation of the system, allow the same local model to generate large-scale organizations similar to those measured empirically.

2.2 Bursts of co-activation underlie the stable functional epochs

In both the bistable and the monostable regimes, the edge CA time series extracted from the simulated BOLD activity are characterized by collective *events* i.e., bursts of co-fluctuations occurring at short intervals of time across the whole brain network (Figure 3A, middle panels). This feature is in accordance with the analysis of the empiric BOLD signals in mice and human resting-state datasets.

When looking at both the dFC_e blocks (Figure 3A, bottom panels) and the BOLD-CA events (Figure 3A, middle panels), we noted that they co-occur in most instance. This observation is non-trivial, since a higher co-activation does not imply a stronger correlation. We note similar co-occurences when processing the BOLD signals of an empiric fMRI dataset in mice and humans.

In order to demonstrate that these events co-occur, we first extracted from the BOLD-CA signals the root sum squared (RSS) time series, which quantifies the amplitude of the edge co-activations at each time point (Figure 3A, blue lines). Then, we partitioned the CA-RSS signal in *events* and *non-events* (respectively above and below the 98th percentile of the RSS values). Finally, we showed that the correlation between any two events is statistically higher than the correlation between events and non-events as well as between couples of non-events (Figure 3B) [1]. Since the correlation between co-activations at different times correspond to the off-diagonal elements of the dFC_e matrix (as shown in Figure 1C), we conclude that bursts of BOLD-CA events account for the highest off-diagonal values in the dFC_e in both theoretical and experimental datasets. We thus looked at the neuronal origin of the collective burst of the hemodynamic co-activations.

[1] The empiric results are pooled over several experimental subjects. In supplementary Figure S2A we show examples of the dFC_e, where times are sorted accordingly to increasing CA amplitude. In supplementary Figure S3B we explore the effect of a different thresholding on Figure 3B in the Human data.

2.3 Neuronal cascades account for functional connectivity dynamics

When looking at the simulated neuronal activity, we note that the largest excursions of some regions' firing rate away from baseline, which we refer to as neuronal *cascades*, often occur in correspondence of the main BOLD-CA events. To visualize this correspondence, we build a raster plot (Figure 3A, top) by z-scoring each firing rate signal $r_n(t)$ and binarizing the activity in every brain region n by assigning a unitary/null value when the signal is above/below a given threshold (e.g., 3 standard deviations). In order to compare the fast neuronal activity with the simulated BOLD signal we average the deviations from baseline in non-overlapping time windows of 2s (corresponding to one BOLD point). The comparison between the neuronal cascades and the BOLD-CA edge time series (respectively top and middle panels in Figure 3A) shows indeed a relationship between the two simulated processes. Remarkably, a similar correspondence is found when analyzing EEG and fMRI signals acquired simultaneously in a resting-state human dataset (example subject in Figure 3A). To characterize this correspondence we first average the raster plots in Figure 3A across all brain regions, defining a time-series of neuronal cascades *magnitude* (red line in Figure 3A). Then, we compare the cascades magnitude with the BOLD-CAs amplitude (RSS, blue line in Figure 4A). In both the monostable and the bistable regimes, the two measures are significantly correlated ($\rho > 0.7$). In Figure 4A (top) we report the correlations between the cascade magnitude and BOLD-CA amplitude across a human cohort. The correlation is carried out by shifting the BOLD time series of a given time-lag. A peak of correlation appears naturally between the two measures when the BOLD signal is shifted by $[0 - 1]$ time points backwards Figure 4A (bottom). Therefore, as expected, the EEG signal precedes the BOLD co-activations by few seconds. Notice that, in general, a shift forward of the BOLD activity results in a rapid loss of correlation.

Finally, to prove a statistical significance of our observations, we show in the Human empiric dataset that the probability that a large neuronal cascade (red dots, marking the points above 98th percentile of the red lines in Figure 3A) is followed by a BOLD-CA event (blue dots, above 98th percentile of the blue lines in Figure 3A) is high when compared to static surrogate models. Namely, we compare the probability in the original dataset (averaged across all the experimental subjects, in green in Figure 4) with the probability that a large neuroelectric cascade is followed by a CA events obtained from time-shuffled and phase-randomized surrogates of the BOLD activity (orange and blue distributions in Figure 4B). The two surrogate models respectively correspond to a random and a completely ordered dynamical scenarios (see Methods section). The probability of a causal relation among EEG and BOLD peaks is also compared with the low probability that a peak of the motion time series follows a neuronal cascade (black line) or precedes a BOLD CA event (dashed red line). The result holds in most instance at the single subject level (Supplementary Figure S3C). We conclude that neuronal cascades play a central role in the complex dynamics of the functional connectivity.

Many questions about the nature of the functional dynamics are still open. Which microscopic mechanisms are responsible for the eruption of neuronal cascades? Does the spatiotemporal evolution of a neuronal cascade contribute in shaping the emergent pattern of BOLD co-activation? In Figure 4C we show the example of a human subject where the largest neuronal cascades subtending bursts of BOLD-CA are very similar throughout the recording. Notably, all the cascades spread into a specific subnetwork (Figure 4D; relative list of brain regions in Figure S5). An in depth exploration of this phenomenon will require further exploration on a larger human cohort.

In the next sections we investigate in deeper detail the large-scale neuroelectric organization in the context of the model. First, we clarify the role of the noisy fluctuations in powering the system and that of the structural connectome in dissipating the energy throughout its channels. Then, we study in detail the neuroelectric activity at the level of the single time series. In

this context, the mechanisms of cascade generation will be discussed. Finally, we show in the synthetic data the pathways in which the neuronal cascades spread and the corresponding evoked functional networks.

2.4 Dynamical evolution as response to perturbations: analysis of the synthetic data

For a decoupled system, the phase plane representation of a network node n, has an 'up' stable focus and a 'down' fixed point (first panel in Figure 5A): in the 'up' state the neurons populating the neural mass exhibit an intense activity with high average firing rate and low average membrane potential; in the 'down' state the local neurons posses low firing rate and strong (negative) membrane potential. As we increase the input current I_{ext} in the decoupled neural mass equations (Figure 5B), the two branches of the V-nullcline move horizontally away from each other, while the r-nullcline remains fixed (Figure 5A). Correspondingly, the location of the stable points in the phase plane shifts and their basins of attraction change in size. In the coupled system, we can approximate the network action over n as an external current I_n (almost constant in our simulations) (Figure 5B). Therefore, the projected phase planes (r_n, V_n) are distorted versions of the decoupled phase plane, where the location of the down fixed point and the up stable focus depends on the structural role that each region plays in the network hierarchy. [2] Poorly connected regions in the connectome receive a weak input current I_n so that the local phase plane is slightly distorted. Instead, regions with high centrality in the connectome, or that are part of strongly connected structural motifs, receive a strong input which causes a greater distortion of the local phase plane.

In absence of noise the neuronal activity in every brain region would rapidly freeze into a stable level of activity (for all the values of the global coupling considered in Figure 2). In our simulation, a frozen dynamics corresponds to each node n settling into a stable state as seen from a local phase plane representation i.e., the 2D projection of the global phase space into the phase plane (r_n, V_n). A random fluctuation provides the first impulse that pushes the system away from a stable state and allows for a richer interaction among the brain regions. Therefore, the random noise can be thought as pumped energy which powers the system. Overall, we can think at the dynamics of the simulated system as a continuous adaptation to the environmental perturbations [3].

In the monostable regime (Figure 2) the low value of the global coupling imposes a weak structural pull over the local dynamics. In this regime it easier to jump from the up stable focus to the down fixed points (following a random perturbation), while a jump from the down to the up state is less probable. Eventually, every region is quickly attracted to the down fixed point. Nonetheless, a non-null probability exists that a region hanging in the down state suddenly jumps in the up state driven by the strongest noisy perturbations. This probability changes depending on the network node we observe, as its role in the structural hierarchy shapes the distance between the fixed points as well as the size of their basins of attraction in the local phase plane representation. In the bistable regime (Figure 2), the global coupling G has a higher value and the local arrangements across the brain network are more evenly distributed between the up and down fixed points. Strongly connected regions receive a strong average input and are maintained in the up stable focus. Vice versa, poorly connected regions fall in the down fixed point. Given the

[2] Despite the small degeneracy effect, describing the activity in every node we will always refer to up and down states.

[3] Rather then the initial values of the state variables r_n and V_n, the dynamics is highly influenced by the random noise which powers the system. In fact, the same noise configuration would rapidly lead the activity to the same exact dynamics, independently of the initial values of the system variables.

low noise level, only a subset of regions (with an intermediate strength of the structural inputs) is capable of jumping between the up and the down states. Summarizing, by affecting the size and the shape of the basins of attraction in the local phase planes, the structure constraints the standard activity of each region into the boundaries of 'what is reachable' by receiving random kicks from the noise.

The structure also determines the way the system re-balances after a perturbation, as it shapes the channels through which the energy is dissipated. Let us imagine a region n which undergoes a sudden transition, from a low to a high firing rate state (i.e., from the down to the up stable point). Accordingly, this region will become 'visible' to the other nodes across the network, as it will start communicating with increased intensity. The system would not be homogeneously affected by such a change in the information routing. Instead, the regions more connected to n would be greatly influenced while the less connected ones would continue their normal activity almost undisturbed. Therefore, following a local phase transition (e.g., from low to high average firing rate of the QIF neurons forming the neural mass), the structural motifs and pathways become the outlets to channel the energy fluctuations in the system.

2.5 The neuronal correlates of the bistable regime

Here, we focus on the neuronal correlates of the bistable regime to understand how the largest neuronal cascades, which we have shown to underlie the functional dynamics, are generated in our system. Let us recall that the local parameters have been fixed so that the local decoupled dynamics is everywhere in the same bistable configuration (Figure 5A, $I_{ext} = 0$). Then, the nodes have been coupled on a realistic connectome (Figure 1A). As we discussed above, the coupling deforms the local phase planes so that the location of the up and down stable points for a given region depends on the structural role it plays in the network. In turn, a different level of activity is associated with a unique role in the communication across the network. Roughly speaking, the dynamics consists of a noisy exploration around the up or the down stable points. Occasionally, if the two stable points in a local phase plane are close enough, a jump between the stable states may occur following a random perturbation.

Looking into each local 2D phase plane projection, we could think of a *separatrix* i.e., a boundary line separating the up and down basins of attraction, as being a dynamical element. In general, its location depends on the amount of input that the region is receiving at a given time and, as already discussed, we expect it to be related to the structural role played by the region in the network.

We can identify five main categories to classify the nodes' dynamics in the bistable regime:

- (D) *down* regions (in light blue in Figure 5C) are stuck into a low firing rate state throughout the duration of the simulation, as the up state is practically unreachable. We can think of the separatrix as being closer to the up state so that, given the amount of random noise, it is very improbable that they will change state. Their dynamics is confined into a low firing rate regime, which makes them poor communicators in the network hierarchy.

- (U) *up* regions (in light red in Figure 5C) always show high firing rate, and constantly contribute to the membrane currents of the neurons across the network. The separatrix lays close to the down state and it is never reached.

- (J) *jumping* regions (in green in Figure 5C) undergo regular local transitions, dwelling for a relatively long time in both low- and high- firing rate states. We can imagine that in the phase space of these regions the separatrix lays somewhere at mid distance between the up and down states. Therefore they have similar probability to jump from up to down and

vice versa. Notice that the timing of the (J) jumps defines a new *slow* time scale for the system. The fact that these jumps occur on a regular basis during the simulation ensures that the time scale is ever-present in the large scale network dynamics.

- (D*) *down-up* regions (in dark blue in Figure 5C) have a stable activity around the down fixed point but–in some occasions–manage to reach the up stable focus for a certain transient time.
- (U*) *up-down* regions (in dark red in Figure 5C) have a stable activity around the up state but are occasionally driven into a short-lived change of state in the down state.

Jumps of the local activity between stable points provoke big shocks throughout the system. In order to understand the impact of a local transition over the large-scale network, let us focus on the equation (6) (in the Methods) defining the rules of communication between the nodes of the network. At each time step, any message starting from a node n is encoded by the firing rate r_n, which enters as an additive input into the membrane potential V_m of a receiving region m (Figure 5B). Then, the message is processed at m as a new input $I > 0$, and its intensity depends on the weight of the structural link W_{nm} connecting the nodes. This causes a shift of the separatrix in the local phase space projection (r_m, V_m). The stronger is the input, the more the separatrix gets closer to the down fixed point, increasing the probability of m hanging in the up stable focus basin of attraction. Notably, when a region changes its state by jumping into the other stable point, its firing rate will drastically change, and this event will cause a major shift of the separatrix lines throughout the network nodes.

Therefore, we expect the nodes of class (J) to provide a relevant driving system for the network, despite they constitute only a small subset in the chosen regime. In fact, compared to the majority of nodes having a stationary activity around a single focus, their frequent jumps have a remarkable effect over the large-scale network. A Principal Component Analysis (PCA) shows indeed that the nodes (J) explain most of the system variance (Figure S4B). However, given their uniform unfold throughout the simulation, the activity of regions (J) rarely grows above few standard deviations from the mean (green in Figure 6B).

Instead, a substantial contribution to the large system deviations from baseline is made by the regions in classes (D*) and (U*) which have a less regular activity. During their occasional excursions in the other stable state, the activity of these regions substantially deviates from the mean (dark red and blue in Figure 6B), and they become active players in the organization of the network.

The central role of the structure in the fate of the local activity is clearly shown by the topographic organization of the average firing rate in the regions across the brain network (Figure 5C). Roughly speaking, peripheral nodes receiving small inputs will remain in the down state, nodes with high centrality receiving a very strong input will stay up, nodes with average structural in-strength will have some probability of jumping across the separatrix. In the economy of the network, there are also other structural features which play an important role. Take the case of a node with jumping potential which is also a hub for the network. Then, its local reshaping will have a wider influence throughout the network. On the other hand, the hubness of the node does not guarantee that in response to its jump some other region will also cross the separatrix. Think of the scenario in which, following a jump of the hub, most of the separatrix lines will be shifted a little, but not enough to allow any crossing. On the contrary, if there exists a subset of nodes with jumping potential and strongly connected among them, then the jump of one will have important consequences within the subnetwork. In order to clarify this point, let us imagine that a group of nodes from class (U*), have very strong links binding them. Then, the occasional jump down of one of these nodes will considerably shift the separatrix of the other (U*) nodes

towards the up stable focus, increasing their probability of jumping down. In this scenario many (U*) nodes could be dragged down one after the other, making after each jump more easy the downhill and producing an *avalanche* (see for example Figure 6B, bottom). During this event, also the nodes (J) get involved, interrupting for some time their regular control over the network. A new mechanism has taken the lead of the system. Let us notice that to some degree the (U*) and (D*) groups are antagonists since the jump of their elements disfavor the jumps in the other class.

Summarizing, we have shown that jumps of the firing rate at local sites are extremely relevant for the unfolding of the microscopic activity across the whole-brain, as they provokes the biggest shocks in the system. Let us recall that a jump entails a rapid reconfiguration of the QIF neurons constituting the Neural Mass (see Methods). Therefore, we can intuitively think of a jump in the average activity of a brain region as a local phase transition. These events can generate a slow time scale in the system if they happen with a certain regularity. In fact, the emergence of a slow rhythm in our system can be traced back to a small subset of regions (J) which throughout the simulation undergo regular local phase transitions, dwelling for a relatively long time in both the up and the down states. These regions lead the baseline evolution of the entire system. In some rare but important occasions this control is overshadowed by large avalanches. An avalanche effect takes place when a sudden local transition brings a typically stable region ((U*) or (D*)) away from baseline activity and induces other regions to reorganize. The cascade goes on until the noise and the structural pressure take the system back to its normal evolution.

2.6 Neuronal cascades and emerging Functional Networks

We finally show that in the bistable regime similar cascades occurring in succession, produce bursts of similar BOLD co-activations and evoke stable resting state networks correlated in time. As we discussed in the last section, the largest avalanches start from the (U*) or the (D*) regions (respectively dark blue and dark red in Figure 5C and Figure 6B) and spread into specific structural channels. Such deviation from baseline activity emerges at the BOLD level as collective co-activations at network edges across the brain. The presence of off-diagonal blocks in the dFC_e (Figure 6A) shows that co-activation patterns are correlated when generated either in the (D*) or in the (U*) regions. In our example the co-activations which generate from avalanches of distinct classes are not correlated. Each CA pattern defines the upper triangular part of an instantaneous functional connectivity iFC (as in Figure 1C). We can extract the associated functional network as the first leading eigenvector of the iFC, whose components are represented as different colors in the brain network plots (Figure 6, left). In the selected epochs, the more a node participated into a neuronal cascade the biggest is its radius in the brain network plots. The same avalanche can re-occur eliciting similar functional networks correlated at distinct times, as it is marked by the off-diagonal blocks of the dFC_e (see the network plots in the first row or those in the second row). Different avalanches elicit different BOLD-CA events which result in uncorrelated functional networks (first versus second row of brain plots).

3 Discussion

Cognitive function requires the coordination of neural activity across many scales, from neurons and circuits to large-scale networks. As such, it is unlikely that an explanatory framework focused upon any single scale will yield a comprehensive theory of brain activity, cognitive function or brain disease. Fast time scales evolve within the quasi-stationary constraints imposed by slow time scales. As the latter change, the organization of the former must change consequently. We demonstrated this principle along the organization of the fast neuroelectric correlates of the slowly evolving large-scale dynamic Functional Connectivity (dFC) patterns for several mammalian species. Large neuronal cascades, defined by collective deviations of the simulated EEG signals away from baseline activity, can emerge as co-activation (CA) BOLD events, i.e. large simultaneous activation at pairs of regions across the brain network. In turn, the intermittent set of BOLD-CA events underlie specific stable FC epochs. Thus, large neuronal cascades have an organizational role in the resting state brain dynamics.

In this work, we have adopted a theory driven approach to reproduce qualitatively the resting state FC, while keeping track of the electric neuronal activity [50]. To address multiscale-phenomena, we maintain the co-existence of microscopic and macroscopic scales of organization. We have constructed a model that maps the activity of an infinite number of coupled neurons, each described by a simple phase-oscillator equation, into the mean field firing rate and membrane potential variables. Future applications allow the possibility of including synaptic dynamics [59, 60], adaptation [61], excitatory versus inhibitory populations [50, 62, 63], among others. Although not giving full access to biophysical processes, as when using detailed single neuron models, the model we used carries a low computational load, enabling the simulation of fMRI-like sessions in TVB while preserving important information about the microscopic neuronal organization (see Methods).

While the debate over the actual nature of functional connectivity dynamics is still open [27, 64, 65], evidence was provided in favor of the dFC as a legitimate measure of the functional evolution. In fact, the temporal unfolding of the FC displays transient epochs of slowdowns and accelerations. The distribution of the FC 'speeds' lies between a completely ordered scenario and a random one, a hallmark of complexity [38]. We found that a large part of the functional information is condensed in large BOLD-CA events, in keeping with previous results [66]. The occurrence of the BOLD-CA events cannot be ascribed to the spectral properties of the BOLD signals nor to motion artifacts [66], which supports a genuine phenomenon. Our results provide an *in silico* support to a bursts-based system dynamics, which might be a general property for a class of high-dimensional systems organized at large spatial and slow temporal scales. Indeed, the dynamics is driven by short activation peaks, rather than by continuous processes, in accordance with previous works showing that the relevant information about the major resting state networks is carried by the largest fluctuations of the fMRI blood oxygenation level-dependent (BOLD) signals [67, 68, 69, 70, 71].

Varying the global couplings in the model, we discovered two regions of the parameter space–defining the monostable and the bistable regimes–where the large-scale organization is qualitatively different e.g., in terms of the statistical properties of the BOLD-CA events (Figure 3B) or in the life-time of the stable functional states (i.e., the size of the dFC blocks in Figure 3A, bottom). The generation of a variety of dynamic regimes from changes in the global 'environmental' parameters is biologically realistic. For example, sleep deprivation is associated with changes in the speed of the FC evolution [72]. Accordingly, distinct features of the dFC should correspond to a different underlying neuroelectric organization (and perhaps to distinct mechanisms of communication across the brain regions [73]). The transition between wakefulness and sleep brain states offers an example of sudden change of the whole-brain dynamics associated with the

microscopic neuroelectric re-organization [74, 75, 76, 77]. In our model, the neuroelectric correlates of the monostable and the bistable regimes define distinct pathways towards a large-scale dynamic organization (Figure 2). Further exploration of the parameter space may reveal new mechanisms of pattern formation.

During the BOLD-CA events the evolution of the FC slows down, as reported by the high correlation between functional states at consecutive times (Figure 3). A slowing down of the dynamics could be associated to longer absorption times of the largest BOLD fluctuations away from baseline activity. An emergent stable FC elicited by a BOLD-CA event can persist for several seconds. The same state can re-appear after few minutes in coincidence with another CA. Therefore, the spontaneous bursts of co-activation at pairs of nodes across the brain highlight special sets of network edges. How the system selects these preferential sets and what triggers the sudden co-fluctuations are open questions, but suggest that large neuronal cascades may play a central role in determining fluctuations in resting, perceptual and cognitive processes. These findings highlight the strong interdependence between the multi-scale neural processes.

In many dynamical systems, slowdowns and large-scale events are typically observed at the transition between different states (or phases) i.e., at the critical point. Critical dynamic systems are characterized by specific properties, including the presence of fluctuations at all spatiotemporal scales [78]. Historically, the hallmark of a critical organization of the brain activity came from the observation of neuronal *avalanches* whose size and duration fit a power-law [79] (see [80] for a 'critical' look at brain criticality). This pioneering work provided proof-of-principle that the science of criticality could be used to inform our understanding of complex patterns of activity in the brain and, by extension, behaviour, even though, with few notable exceptions [81, 82], these two streams of research have preceded largely in parallel. Establishing the presence of critical instabilities in neurological disorders opens a number of novel therapeutic and diagnostic windows (for review, see [83]). Schizophrenia for instance is associated with less suppression of activity in the default-mode network when subjects engage in external tasks [84, 85, 86, 87]. These examples remain sparse and often disconnected across domains, which renders the need to an overarching framework across scales important. Our model makes a constructive contribution in this sense. Neuronal avalanches are observed across orders of magnitude by analyzing the simulated EEG signals (Supplementary Figure S4C). Importantly, both regimes feature rare large-scale events. In order to compare the fast EEG and the slower BOLD signals, we focused on the average EEG deviations from baseline activity occurring within non-overlapping windows, each corresponding to a single BOLD point. In other words, instead of focusing on the size and duration of the neuronal avalanches, we analyzed their collective occurrence at the resolution of seconds, which we refer to as neuronal cascades. We showed that the cascade magnitude is correlated to the BOLD co-activation amplitude (Figure 3B). In particular, in the empiric human dataset we observe a rapid drop of this correlation when the BOLD activity is shifted backward w.r.t. the EEG signal. This fact makes our result more robust, since we expect a change of the BOLD activity to happen *after* a sustained neuroelectric activity.

Then, we showed that the BOLD CA peaks follow from the largest neuronal cascades with a significant probability (Figure 4C). The result is reproducible at the single subject level (Supplementary Figure S3C) and it is not linked to motion artifacts. The likelihood of this microscopic influence over the hemodynamic activity is compared to the probability obtained from two static BOLD surrogates. In the time-shuffled surrogate, the activity consists of random fluctuations around a stable FC. In the phase-randomized surrogate any causal dynamics is disrupted, but the static FC is preserved. Notice that in both surrogates the BOLD-CA events are not destroyed, but their timing is changed (see supplementary Figure S3A). Then, the original location of the BOLD CA peaks is significantly related to the largest neuronal cascades and subtends a complex dynamics.

In the empiric data set, not all the neuronal cascades give rise to BOLD CAs, and not all the BOLD CAs are preceded by large neuronal cascades. In the cases in which they co-occur, one could hypothesize that the stable FC state evoked by a CA event is related to the specific structural channels in which the neuronal cascade spreads. In fact, we showed in the simulated data that the largest neuronal cascades underlie specific functional patterns (Figure 6), depending on the location of the avalanche onset. Also, the observation that the same avalanche appears at regular intervals in Figure 6 suggest that the re-occurrence of the same stable patterns in time could be traced back to the increased probability of the same cascade to occur following a first large event, in the same way an after-shock follows the main earthquake. More generally, aspects of the functional dynamics phenomenology might be be inherited by the (seemingly) critical properties of the neuronal activity. Traces of criticality were in fact observed also in the hemodynamic activity [67]. The above hypotheses require further exploration on larger empiric data sets. In the model, we have shown that the mechanistic origin of the largest avalanches can be understood ultimately by the interplay between the local dynamics, structural constraints and stochastic events. A preliminary analysis on a single human subject shows that the neuronal avalanches occurring in correspondence of BOLD-CA events spread in specific network sites which are similar despite appearing at distant times (Figure 4C-D).

The present work paves the way for a new understanding of the whole-brain functional dynamics and links it to the field of critical phenomena.

4 Materials and Methods

4.1 Empirical Mice and Human data sets

The connectome used for the simulations was extracted using The Virtual Mouse Brain pipeline described in [42], which processes the tracer experiments performed at the Allen Institute [51]. There, adult male C57Bl/6J mice are injected in specific brain regions with recombinant adeno-associated virus, which expresses the EGFP anterograde tracer. In each experiment, the tracer migration signal is detected by a serial two-photon tomography system. The anterograde tracing provides information about the axonal projections starting at the injected site. We define the injection density of the source region as the number of infected pixels normalized by the total number of pixels in the region. Similarly, the projection density is defined in every region as the number of pixels detected in the target region following an injection at the source, normalized by the total number of pixels belonging to the target region. The tracer-based connectome is built by averaging over injection experiments performed in the right brain areas and targeting regions in ipsilateral and contralateral hemispheres. Through the Allen Connectivity Builder interface in TVB we parceled the brain in 104 anatomical regions of interest (ROIs, table in Figure S4A). Then, we defined the connection strength between source region i and target region j i.e., the link ij, as the ratio between the projection density at j and the injection density at i. The tracer connectome, with links normalized between 0 and 1 is shown in Figure 1A.

The empirical fMRI mice dataset was imported from the publicly available collection [88]. For our analysis we used the cohort of 20 control wild-type (resting) animals registered in the sub-dataset [89]. The data was previously preprocessed according to a common pipeline, and registered on the Allen volumetric atlas. In our analysis we considered the activity in those voxels corresponding to the imported Allen connectome (Table in Figure S4A). The empiric dataset did not distinguish between specific parts (e.g.,ventral and dorsal) of certain brain regions (blue and red pairs in Table in Figure S4A). A unique time series was associated to each of these pairs of regions.

The empirical EEG/fMRI dataset was acquired and preprocessed at Charité - Universitätsmedizin Berlin [90] and made available in online repository[4] [49]. In summary, from a larger cohort (49 subjects, 18-80 years), 15 youngest subjects (18-31 years) were selected based on the quality of the EEG recording after correction of the MR artifacts. For each subject, diffusion-weighted MRI, T1-weighted MRI, and EEG-fMRI in resting state paradigm were obtained. The T1-weighted image was used to parcellate the cortical gray matter into 68 regions according to the Desikan-Killiany atlas [91] (list of regions in Figure S5A). This definition of regions was then used to estimate the structural connectivity from the dw-MRI data [92], and to extract the regional average time series from the fMRI data. The EEG data (Easy-cap; 64 channels, MR compatible) was treated with a high pass filter at 1.0 Hz followed with MR imaging acquisition artefact removal using Analyser 2.0 (v2.0.2.5859, Brain Products, Gilching, Germany). Resulting sensor-level time series was downsampled to 200 Hz and low pass filtered to 30 Hz before correction for physiological artifacts (ballistocardiogram, muscle activity). Next, EEG source imaging was performed to obtain projected activity on the cortical surface, and averaged within the 68 regions of the Desikan-Killiany parcellation. See [90] for detailed description of both fMRI and EEG processing. In Figure 4 the EEG and fMRI data are compared with a representative motion time series defined as the first principal component of the time series of the 6 motion degrees of freedom resulting from the FSL MCFLIRT head movement correction step.

[4] https://osf.io/mndt8/

4.2 Neural Mass Model

The dynamics of a brain region of interest (i.e., a node in the network) is described by a Neural Mass Model (NMM) derived analytically as the limit of infinitely all-to-all coupled θ-neuron phase oscillators, whose dynamics is equivalent to that of quadratic integrate-and-fire (QIF) neurons (Figure 1B) [50]. The i-th neuron is described by the equation

$$\dot{V}_i(t) = V_i^2(t) + \eta_i + J\bar{s}(t) + I(t) \quad \text{if} \quad V_i \geq V_p \quad \text{then} \quad V_r \leftarrow V_i. \tag{1}$$

As the membrane potential reaches a peak value V_p, it resets to V_r. The limit $V_p = -V_r \to \infty$ is considered. The parameter η_i is the neuron excitability, and it enters as an heterogeneous current in the membrane potential. A time-dependent current $I(t)$ homogeneously affects all the neurons in the neural mass. The synaptic activation $s(t)$ of a single neuron respects the equation $Q \cdot s(t) = \sum_k \delta(t - t_k)$, being $Q = (1 - \tau \frac{\mathrm{d}}{\mathrm{d}t})$ and t_k the arrival time of the presynaptic action potential. The neuronal coupling among N QIF neurons inside a neural mass is given by the average synaptic activation $\bar{s}(t) = \frac{1}{N}\sum_{j>1}^{N} s(t)$ scaled by the synaptic weight J. Assuming a Lorentzian distribution of the membrane potentials across the coupled neuronal population it is possible to perform the $N \to \infty$ limit exactly according to the Ott-Antonsen ansatz [93]. Also the heterogeneous currents are distributed according to a Lorentzian distribution with width at mid height Δ and peak location η. After the limit we can describe the activity in a neural mass n in terms of the average membrane potential $V_n(t)$ and the average firing rate $r_n(t)$ (which corresponds to $\bar{s}(t)$ in the limit $\tau \to 0$). The dynamics associated to a local network node is then described by the following NMM equations

$$\dot{r}_n(t) = \frac{\Delta}{\pi} + 2r_n(t)V_n(t), \tag{2}$$

$$\dot{V}_n(t) = V_n^2(t) + \eta + Jr_n(t) - \pi^2 r_n^2(t) + I(t). \tag{3}$$

The synaptic weight $J = 14.5$, the average neuronal excitability $\eta = -4.6$, and the spread of the heterogeneous noise distribution $\Delta = 0.7$, are homogeneously tuned so that each decoupled node is in a bistable regime with a 'down' fixed point and an 'up' stable focus in the 2D phase space (Figure 5A, $I_{ext} = 0$). Differently from standard NMMs, the chosen model keeps track of the internal amount of synchronization of the constituent neurons by preserving the analytic form of the Kuramoto parameter [48]

$$Z_n(t) = |\sum_i \exp(i\theta_i)| = K_n(t)\exp(i\theta_n(t)), \tag{4}$$

during the thermodynamic limit [5]. Here, K_n and θ_n are the average amount of synchronization and the average phase of the neurons in the node n. The real and imaginary components of Z_n are connected to the average membrane potential V_n and firing rate r_n of the neural population n via the relation

$$Z_n = \frac{1 - W_n^\star}{1 + W_n^\star}, \qquad W_n \equiv \pi r_n + iV_n. \tag{5}$$

4.3 Connectome based large-scale Network Modeling

The local model is then coupled over an empirically extracted connectome (Figure 1A). The coupling term enters as an additive current in the average membrane potential equations (see

[5] The θ_i-representation of the QIF equations can be achieved from (1) by a simple change of variables $V_i = \tan(\theta_i/2)$

also Figure 5B)

$$I(t) = G \sum_{m \neq n} W_{nm} r_m(t - \tau_{nm}) \tag{6}$$

The global coupling parameter G sets the impact of the connectivity matrix W_{nm} over the local dynamics. The time delay $\tau_{nm} = l_{nm}/s$ is given by the tract length between nodes n and m divided by the average conduction speed which we set to a realistic value $s = 4\ m/s$. Since the firing rate is by definition greater than or equal to zero, all the interactions are excitatory.

The numeric integration of the nodal equations over the network is performed using The Virtual Brain (TVB) open access platform [40]. The solution of the coupled system consist of a neuroelectric raw dataset describing the evolution of the variables $(r_n(t), V_n(t))$ in each region n of the connectome. These variables–or equivalently the Kuramoto parameter $Z_n(t) = K_n(t)exp(i\theta_n(t))$–are our measure of the microscopic activity. The sampling rate of these neuroelectric variables is set to 1000Hz. The surrogate BOLD activity $B_n(t)$ in each region is derived by filtering the membrane potential with the Balloon-Windkessel model [52] (default values implemented in TVB). We use a repetition time of 2 seconds so that the BOLD rate is 0.5 Hz.

4.4 Time dependent functional connectivity

To quantify the temporal evolution of the brain connectivity, we have employed two approaches: windowed dynamical functional connectivity (dFC_w), and edge dynamical functional connectivity (dFC_e). Let us denote $B_n(t)$ as the regional BOLD time-series for each node $n = 1 \dots N$. To compute the dFC_w [25, 38], we first obtain the series of functional connectivity matrices $FC(w)$ at each sliding window $w = 1 \dots W$, defined as the correlation matrices for the segments $B_n(t)|_{t_w}^{t_w+\tau}$ (in the example Figure S1A we fix the window size $\tau = 60s$ and window step $2s$). Next we correlate the vectorized upper triangular parts of the $FC(w)$ matrices at different time windows to obtain the dFC_w matrix

$$dFC_w(w_i, w_j) = corr\left[triu(FC(w_i), triu(FC(w_j))\right]. \tag{7}$$

On the other hand, the computation of the dFC_e starts with z-scoring the BOLD time series $z_n = \frac{B_n - \mu_n}{\sigma_n}$. The edge time series is then computed as element wise multiplication along time for each pair of regions $E_{nm}(t) = z_n(t)z_m(t)$ for $n, m = 1 \dots N$ (see Figure 1C). Next, for each pair of time points t_1, t_2 we compute the correlation of the edge vectors as

$$dFC_e(t_i, t_j) = corr(E_{nm}(t_i), E_{nm}(t_j)). \tag{8}$$

While both dFC variants are similar, the main difference lies in the scope of z-scoring of the time series B_n. In the case of dFC_e the z-score z_n is computed from the whole time series, whereas in the dFC_w the z-score is performed within the Pearson correlation in each time window $[t_w, t_w+\tau]$ separately. To check the correspondence of the dFC_e and dFC_w matrices, we have also computed a hybrid dFC from the edge time series E_{nm}. Here we select the segments $w = 1 \dots W$ of the edge time series $E_{nm}(t)$ for $t_w \leq t \leq t_w+\tau$. Next, to keep the global scope of the z-scoring, we compute the $FC'(w)$ as a sum $FC(w) = \sum_{t_w}^{t_w+\tau} E_{nm}(t)$. Lastly, we compute the hybrid dFC matrix from the $FC'(w)$ vectors as

$$dFC_h(w_i, w_j) = corr\left[FC'(w_i), FC'(w_j)\right]. \tag{9}$$

See Figure S1 for a schema illustrating the computation of all three variants of the dFC, and for comparison of the dFC variants in empirical and simulated data.

4.5 Surrogate BOLD models

In order to compare our results in Figure 4B with the null-hypotheses of a random evolution and of inter-regional stationarity of the FC, we build time-shuffled and phase-randomized surrogates of the FC dynamics, respectively. The time-shuffled surrogate is obtained by randomizing the order of the instantaneous functional connectivities $iFC(t)$ i.e., the columns of the edge CA time series $E_{ij}(t)$ (see Figure 1C). According to [27] the phase randomized surrogate is obtained by adding a uniformly distributed random phase to each frequency of the Fourier transformed signal, and subsequently retrieving the phase randomized signals by anti-Fourier transform. Importantly, the phase shift is different at every time point but it is uniformly applied to all the brain regions, so that the bursts of co-activation are shifted in time (but not destroyed, Figure S3A) and the static FC is preserved. The coherent fluctuations around the stationary FC, however, are destroyed. For more details see also [94].

References

[1] Michael D. Greicius, Ben Krasnow, Allan L. Reiss, and Vinod Menon. Functional connectivity in the resting brain: A network analysis of the default mode hypothesis. *Proceedings of the National Academy of Sciences*, 100(1):253–258, 2003.

[2] Ming Song, Yuan Zhou, Jun Li, Yong Liu, Lixia Tian, Chunshui Yu, and Tianzi Jiang. Brain spontaneous functional connectivity and intelligence. *NeuroImage*, 41(3):1168 – 1176, 2008.

[3] Martijn P. van den Heuvel, Cornelis J. Stam, René S. Kahn, and Hilleke E. Hulshoff Pol. Efficiency of functional brain networks and intellectual performance. *Journal of Neuroscience*, 29(23):7619–7624, 2009.

[4] Pablo Barttfeld, Lynn Uhrig, Jacobo D Sitt, Mariano Sigman, Béchir Jarraya, and Stanislas Dehaene. Signature of consciousness in the dynamics of resting-state brain activity. *Proceedings of the National Academy of Sciences*, 112(3):887–892, 2015.

[5] Katell Mevel, Gaël Chételat, Francis Eustache, and Béatrice Desgranges. The default mode network in healthy aging and alzheimer's disease. *International journal of Alzheimer's disease*, 2011, 2011.

[6] Cheryl Grady. The cognitive neuroscience of ageing. *Nature Reviews Neuroscience*, 13(7):491–505, Jul 2012.

[7] Luiz Kobuti Ferreira, Ana Carolina Brocanello Regina, Natasa Kovacevic, Maria da Graça Morais Martin, Pedro Paim Santos, Camila de Godoi Carneiro, Daniel Shikanai Kerr, Edson Amaro Jr, Anthony Randal McIntosh, and Geraldo F Busatto. Aging effects on whole-brain functional connectivity in adults free of cognitive and psychiatric disorders. *Cerebral cortex*, 26(9):3851–3865, 2016.

[8] Stephen M Smith, Thomas E Nichols, Diego Vidaurre, Anderson M Winkler, Timothy EJ Behrens, Matthew F Glasser, Kamil Ugurbil, Deanna M Barch, David C Van Essen, and Karla L Miller. A positive-negative mode of population covariation links brain connectivity, demographics and behavior. *Nature neuroscience*, 18(11):1565–1567, 2015.

[9] Raphaël Liégeois, Jingwei Li, Ru Kong, Csaba Orban, Dimitri Van De Ville, Tian Ge, Mert R Sabuncu, and BT Thomas Yeo. Resting brain dynamics at different timescales capture distinct aspects of human behavior. *Nature communications*, 10(1):1–9, 2019.

[10] Danielle S. Bassett, Brent G. Nelson, Bryon A. Mueller, Jazmin Camchong, and Kelvin O. Lim. Altered resting state complexity in schizophrenia. *NeuroImage*, 59(3):2196–2207, Feb 2012. 22008374[pmid].

[11] Jeffrey S. Anderson, Jared A. Nielsen, Alyson L. Froehlich, Molly B. DuBray, T. Jason Druzgal, Annahir N. Cariello, Jason R. Cooperrider, Brandon A. Zielinski, Caitlin Ravichandran, P. Thomas Fletcher, Andrew L. Alexander, Erin D. Bigler, Nicholas Lange, and Janet E. Lainhart. Functional connectivity magnetic resonance imaging classification of autism. *Brain : a journal of neurology*, 134(Pt 12):3742–3754, Dec 2011. 22006979[pmid].

[12] Andrew T. Drysdale, Logan Grosenick, Jonathan Downar, Katharine Dunlop, Farrokh Mansouri, Yue Meng, Robert N. Fetcho, Benjamin Zebley, Desmond J. Oathes, Amit Etkin,

Alan F. Schatzberg, Keith Sudheimer, Jennifer Keller, Helen S. Mayberg, Faith M. Gunning, George S. Alexopoulos, Michael D. Fox, Alvaro Pascual-Leone, Henning U. Voss, B. J. Casey, Marc J. Dubin, and Conor Liston. Resting-state connectivity biomarkers define neurophysiological subtypes of depression. *Nature medicine*, 23(1):28–38, Jan 2017. 27918562[pmid].

[13] Kun Wang, Meng Liang, Liang Wang, Lixia Tian, Xinqing Zhang, Kuncheng Li, and Tianzi Jiang. Altered functional connectivity in early alzheimer's disease: A resting-state fmri study. *Human Brain Mapping*, 28(10):967–978, 2007.

[14] Martin Gorges, Hans-Peter Mueller, Dorothée Lulé, Elmar H Pinkhardt, Albert C Ludolph, Jan Kassubek, LANDSCAPE Consortium, et al. To rise and to fall: functional connectivity in cognitively normal and cognitively impaired patients with parkinson's disease. *Neurobiology of Aging*, 36(4):1727–1735, 2015.

[15] Jonathan D Power, Alexander L Cohen, Steven M Nelson, Gagan S Wig, Kelly Anne Barnes, Jessica A Church, Alecia C Vogel, Timothy O Laumann, Fran M Miezin, Bradley L Schlaggar, et al. Functional network organization of the human brain. *Neuron*, 72(4):665–678, 2011.

[16] Michael D Fox and Marcus E Raichle. Spontaneous fluctuations in brain activity observed with functional magnetic resonance imaging. *Nature reviews neuroscience*, 8(9):700–711, 2007.

[17] Justin L Vincent, Gaurav H Patel, Michael D Fox, Abraham Z Snyder, Justin T Baker, David C Van Essen, John M Zempel, Lawrence H Snyder, Maurizio Corbetta, and Marcus E Raichle. Intrinsic functional architecture in the anaesthetized monkey brain. *Nature*, 447(7140):83–86, 2007.

[18] Hanbing Lu, Qihong Zou, Hong Gu, Marcus E Raichle, Elliot A Stein, and Yihong Yang. Rat brains also have a default mode network. *Proceedings of the National Academy of Sciences*, 109(10):3979–3984, 2012.

[19] Jaymin Upadhyay, Scott J Baker, Prasant Chandran, Loan Miller, Younglim Lee, Gerard J Marek, Unal Sakoglu, Chih-Liang Chin, Feng Luo, Gerard B Fox, et al. Default-mode-like network activation in awake rodents. *PloS one*, 6(11):e27839, 2011.

[20] Francesco Sforazzini, Adam J Schwarz, Alberto Galbusera, Angelo Bifone, and Alessandro Gozzi. Distributed bold and cbv-weighted resting-state networks in the mouse brain. *Neuroimage*, 87:403–415, 2014.

[21] James M Stafford, Benjamin R Jarrett, Oscar Miranda-Dominguez, Brian D Mills, Nicholas Cain, Stefan Mihalas, Garet P Lahvis, K Matthew Lattal, Suzanne H Mitchell, Stephen V David, et al. Large-scale topology and the default mode network in the mouse connectome. *Proceedings of the National Academy of Sciences*, 111(52):18745–18750, 2014.

[22] Alessandro Gozzi and Adam J Schwarz. Large-scale functional connectivity networks in the rodent brain. *Neuroimage*, 127:496–509, 2016.

[23] Joanes Grandjean, Carola Canella, Cynthia Anckaerts, Gülebru Ayrancı, Salma Bougacha, Thomas Bienert, David Buehlmann, Ludovico Coletta, Daniel Gallino, Natalia Gass, et al. Common functional networks in the mouse brain revealed by multi-centre resting-state fmri analysis. *Neuroimage*, 205:116278, 2020.

[24] Enzo Tagliazucchi, Frederic Von Wegner, Astrid Morzelewski, Verena Brodbeck, and Helmut Laufs. Dynamic bold functional connectivity in humans and its electrophysiological correlates. *Frontiers in human neuroscience*, 6:339, 2012.

[25] Elena A Allen, Eswar Damaraju, Sergey M Plis, Erik B Erhardt, Tom Eichele, and Vince D Calhoun. Tracking whole-brain connectivity dynamics in the resting state. *Cerebral cortex*, 24(3):663–676, 2014.

[26] Jian Qin, Shan-Guang Chen, Dewen Hu, Ling-Li Zeng, Yi-Ming Fan, Xiao-Ping Chen, and Hui Shen. Predicting individual brain maturity using dynamic functional connectivity. *Frontiers in human neuroscience*, 9:418, 2015.

[27] Rikkert Hindriks, Mohit H Adhikari, Yusuke Murayama, Marco Ganzetti, Dante Mantini, Nikos K Logothetis, and Gustavo Deco. Can sliding-window correlations reveal dynamic functional connectivity in resting-state fmri? *Neuroimage*, 127:242–256, 2016.

[28] Maria Giulia Preti and Dimitri Van De Ville. Dynamics of functional connectivity at high spatial resolution reveal long-range interactions and fine-scale organization. *Scientific reports*, 7(1):1–12, 2017.

[29] Joanes Grandjean, Maria Giulia Preti, Thomas AW Bolton, Michaela Buerge, Erich Seifritz, Christopher R Pryce, Dimitri Van De Ville, and Markus Rudin. Dynamic reorganization of intrinsic functional networks in the mouse brain. *Neuroimage*, 152:497–508, 2017.

[30] Javier Gonzalez-Castillo and Peter A Bandettini. Task-based dynamic functional connectivity: Recent findings and open questions. *Neuroimage*, 180:526–533, 2018.

[31] R Matthew Hutchison, Thilo Womelsdorf, Elena A Allen, Peter A Bandettini, Vince D Calhoun, Maurizio Corbetta, Stefania Della Penna, Jeff H Duyn, Gary H Glover, Javier Gonzalez-Castillo, et al. Dynamic functional connectivity: promise, issues, and interpretations. *Neuroimage*, 80:360–378, 2013.

[32] Enrique CA Hansen, Demian Battaglia, Andreas Spiegler, Gustavo Deco, and Viktor K Jirsa. Functional connectivity dynamics: modeling the switching behavior of the resting state. *Neuroimage*, 105:525–535, 2015.

[33] Eswar Damaraju, Elena A Allen, Aysenil Belger, Judith M Ford, S McEwen, DH Mathalon, BA Mueller, GD Pearlson, SG Potkin, A Preda, et al. Dynamic functional connectivity analysis reveals transient states of dysconnectivity in schizophrenia. *NeuroImage: Clinical*, 5:298–308, 2014.

[34] Barnaly Rashid, Eswar Damaraju, Godfrey D Pearlson, and Vince D Calhoun. Dynamic connectivity states estimated from resting fmri identify differences among schizophrenia, bipolar disorder, and healthy control subjects. *Frontiers in human neuroscience*, 8:897, 2014.

[35] Jianpo Su, Hui Shen, Ling-Li Zeng, Jian Qin, Zhening Liu, and Dewen Hu. Heredity characteristics of schizophrenia shown by dynamic functional connectivity analysis of resting-state functional mri scans of unaffected siblings. *Neuroreport*, 27(11):843–848, 2016.

[36] Yuhui Du, Godfrey D Pearlson, Dongdong Lin, Jing Sui, Jiayu Chen, Mustafa Salman, Carol A Tamminga, Elena I Ivleva, John A Sweeney, Matcheri S Keshavan, et al. Identifying dynamic functional connectivity biomarkers using gig-ica: Application to schizophrenia, schizoaffective disorder, and psychotic bipolar disorder. *Human brain mapping*, 38(5):2683–2708, 2017.

[37] Maria Giulia Preti, Thomas AW Bolton, and Dimitri Van De Ville. The dynamic functional connectome: State-of-the-art and perspectives. *Neuroimage*, 160:41–54, 2017.

[38] Demian Battaglia, Thomas Boudou, Enrique C.A. Hansen, Diego Lombardo, Sabrina Chettouf, Andreas Daffertshofer, Anthony R. McIntosh, Joelle Zimmermann, Petra Ritter, and Viktor Jirsa. Dynamic functional connectivity between order and randomness and its evolution across the human adult lifespan. *NeuroImage*, 222:117156, 2020.

[39] Joshua Faskowitz, Farnaz Zamani Esfahlani, Youngheun Jo, Olaf Sporns, and Richard F. Betzel. Edge-centric functional network representations of human cerebral cortex reveal overlapping system-level architecture. *Nature Neuroscience*, October 2020.

[40] Paula Sanz Leon, Stuart A Knock, M Marmaduke Woodman, Lia Domide, Jochen Mersmann, Anthony R McIntosh, and Viktor Jirsa. The virtual brain: a simulator of primate brain network dynamics. *Frontiers in neuroinformatics*, 7:10, 2013.

[41] Paula Sanz-Leon, Stuart A Knock, Andreas Spiegler, and Viktor K Jirsa. Mathematical framework for large-scale brain network modeling in the virtual brain. *Neuroimage*, 111:385–430, 2015.

[42] Francesca Melozzi, Marmaduke M Woodman, Viktor K Jirsa, and Christophe Bernard. The virtual mouse brain: a computational neuroinformatics platform to study whole mouse brain dynamics. *Eneuro*, 4(3), 2017.

[43] Kong-Fatt Wong and Xiao-Jing Wang. A recurrent network mechanism of time integration in perceptual decisions. *Journal of Neuroscience*, 26(4):1314–1328, 2006.

[44] Gustavo Deco, Viktor K. Jirsa, Peter A. Robinson, Michael Breakspear, and Karl Friston. The dynamic brain: From spiking neurons to neural masses and cortical fields. *PLOS Computational Biology*, 4(8):1–35, 08 2008.

[45] Gustavo Deco, Kevin M Aquino, Aurina Arnatkeviciute, Stuart Oldham, Kristina Sabaroedin, Nigel C Rogasch, Morten L Kringelbach, and Alex Fornito. Dynamical consequences of regional heterogeneity in the brains transcriptional landscape. *bioRxiv*, 2020.

[46] Roxana A Stefanescu and Viktor K Jirsa. A low dimensional description of globally coupled heterogeneous neural networks of excitatory and inhibitory neurons. *PLoS Comput Biol*, 4(11):e1000219, 2008.

[47] Ben H Jansen and Vincent G Rit. Electroencephalogram and visual evoked potential generation in a mathematical model of coupled cortical columns. *Biological cybernetics*, 73(4):357–366, 1995.

[48] Yoshiki Kuramoto. *Chemical oscillations, waves, and turbulence*. Courier Corporation, 2003.

[49] Michael Schirner. Hybrid brain model data, Sep 2018.

[50] Ernest Montbrió, Diego Pazó, and Alex Roxin. Macroscopic description for networks of spiking neurons. *Physical Review X*, 5(2):021028, 2015.

[51] Seung Wook Oh, Julie A Harris, Lydia Ng, Brent Winslow, Nicholas Cain, Stefan Mihalas, Quanxin Wang, Chris Lau, Leonard Kuan, Alex M Henry, et al. A mesoscale connectome of the mouse brain. *Nature*, 508(7495):207–214, 2014.

[52] Karl J Friston, Andrea Mechelli, Robert Turner, and Cathy J Price. Nonlinear responses in fmri: the balloon model, volterra kernels, and other hemodynamics. *NeuroImage*, 12(4):466–477, 2000.

[53] Waqas Majeed, Matthew Magnuson, Wendy Hasenkamp, Hillary Schwarb, Eric H Schumacher, Lawrence Barsalou, and Shella D Keilholz. Spatiotemporal dynamics of low frequency bold fluctuations in rats and humans. *Neuroimage*, 54(2):1140–1150, 2011.

[54] Stephen M Smith, Karla L Miller, Steen Moeller, Junqian Xu, Edward J Auerbach, Mark W Woolrich, Christian F Beckmann, Mark Jenkinson, Jesper Andersson, Matthew F Glasser, et al. Temporally-independent functional modes of spontaneous brain activity. *Proceedings of the National Academy of Sciences*, 109(8):3131–3136, 2012.

[55] Martin A Lindquist, Yuting Xu, Mary Beth Nebel, and Brain S Caffo. Evaluating dynamic bivariate correlations in resting-state fmri: a comparison study and a new approach. *NeuroImage*, 101:531–546, 2014.

[56] Fikret Işik Karahanoğlu and Dimitri Van De Ville. Transient brain activity disentangles fmri resting-state dynamics in terms of spatially and temporally overlapping networks. *Nature communications*, 6(1):1–10, 2015.

[57] James M Shine, Oluwasanmi Koyejo, Peter T Bell, Krzysztof J Gorgolewski, Moran Gilat, and Russell A Poldrack. Estimation of dynamic functional connectivity using multiplication of temporal derivatives. *NeuroImage*, 122:399–407, 2015.

[58] Michael W Cole, Takuya Ito, Douglas Schultz, Ravi Mill, Richard Chen, and Carrisa Cocuzza. Task activations produce spurious but systematic inflation of task functional connectivity estimates. *NeuroImage*, 189:1–18, 2019.

[59] Stephen Coombes and Áine Byrne. Next generation neural mass models. In *Nonlinear Dynamics in Computational Neuroscience*, pages 1–16. Springer, 2019.

[60] Halgurd Taher, Alessandro Torcini, and Simona Olmi. Exact neural mass model for synaptic-based working memory. *arXiv preprint arXiv:2010.07071*, 2020.

[61] Richard Gast, Helmut Schmidt, and Thomas R Knösche. A mean-field description of bursting dynamics in spiking neural networks with short-term adaptation. *Neural Computation*, 32(9):1615–1634, 2020.

[62] Carlo R Laing. Phase oscillator network models of brain dynamics. *Computational models of brain and behavior*, pages 505–517, 2017.

[63] Grégory Dumont and Boris Gutkin. Macroscopic phase resetting-curves determine oscillatory coherence and signal transfer in inter-coupled neural circuits. *PLOS Computational Biology*, 15(5):e1007019, May 2019.

[64] Timothy O Laumann, Abraham Z Snyder, Anish Mitra, Evan M Gordon, Caterina Gratton, Babatunde Adeyemo, Adrian W Gilmore, Steven M Nelson, Jeff J Berg, Deanna J Greene, et al. On the stability of bold fmri correlations. *Cerebral cortex*, 27(10):4719–4732, 2017.

[65] Raphael Liegeois, Timothy O Laumann, Abraham Z Snyder, Juan Zhou, and BT Thomas Yeo. Interpreting temporal fluctuations in resting-state functional connectivity mri. *Neuroimage*, 163:437–455, 2017.

[66] Farnaz Zamani Esfahlani, Youngheun Jo, Joshua Faskowitz, Lisa Byrge, Daniel P. Kennedy, Olaf Sporns, and Richard F. Betzel. High-amplitude cofluctuations in cortical activity drive functional connectivity. *Proceedings of the National Academy of Sciences*, 2020.

[67] Enzo Tagliazucchi, Pablo Balenzuela, Daniel Fraiman, and Dante R Chialvo. Criticality in large-scale brain fmri dynamics unveiled by a novel point process analysis. *Frontiers in physiology*, 3:15, 2012.

[68] Xiao Liu and Jeff H Duyn. Time-varying functional network information extracted from brief instances of spontaneous brain activity. *Proceedings of the National Academy of Sciences*, 110(11):4392–4397, 2013.

[69] Thomas W Allan, Susan T Francis, Cesar Caballero-Gaudes, Peter G Morris, Elizabeth B Liddle, Peter F Liddle, Matthew J Brookes, and Penny A Gowland. Functional connectivity in mri is driven by spontaneous bold events. *PloS one*, 10(4):e0124577, 2015.

[70] Ignacio Cifre, Mahdi Zarepour, Silvina G Horovitz, Sergio Cannas, and Dante R Chialvo. On why a few points suffice to describe spatiotemporal large-scale brain dynamics. *arXiv preprint arXiv:1707.00759*, 2017.

[71] Daniel Gutierrez-Barragan, M Albert Basson, Stefano Panzeri, and Alessandro Gozzi. Infraslow state fluctuations govern spontaneous fmri network dynamics. *Current Biology*, 29(14):2295–2306, 2019.

[72] Diego Lombardo, Catherine Cassé-Perrot, Jean-Philippe Ranjeva, Arnaud Le Troter, Maxime Guye, Jonathan Wirsich, Pierre Payoux, David Bartrés-Faz, Régis Bordet, Jill C Richardson, et al. Modular slowing of resting-state dynamic functional connectivity as a marker of cognitive dysfunction induced by sleep deprivation. *BioRxiv*, 2020.

[73] Demian Battaglia and Andrea Brovelli. Functional connectivity and neuronal dynamics: insights from computational methods. In *The Cognitive Neurosciences*. 2020.

[74] Mélanie Boly, Vincent Perlbarg, Guillaume Marrelec, Manuel Schabus, Steven Laureys, Julien Doyon, Mélanie Pélégrini-Issac, Pierre Maquet, and Habib Benali. Hierarchical clustering of brain activity during human nonrapid eye movement sleep. *Proceedings of the National Academy of Sciences*, 109(15):5856–5861, 2012.

[75] Linda J Larson-Prior, John M Zempel, Tracy S Nolan, Fred W Prior, Abraham Z Snyder, and Marcus E Raichle. Cortical network functional connectivity in the descent to sleep. *Proceedings of the National Academy of Sciences*, 106(11):4489–4494, 2009.

[76] Enzo Tagliazucchi, Nicolas Crossley, Edward T Bullmore, and Helmut Laufs. Deep sleep divides the cortex into opposite modes of anatomical–functional coupling. *Brain Structure and Function*, 221(8):4221–4234, 2016.

[77] Mazen El-Baba, Daniel J Lewis, Zhuo Fang, Adrian M Owen, Stuart M Fogel, and J Bruce Morton. Functional connectivity dynamics slow with descent from wakefulness to sleep. *PloS one*, 14(12):e0224669, 2019.

[78] Luca Cocchi, Leonardo L Gollo, Andrew Zalesky, and Michael Breakspear. Criticality in the brain: A synthesis of neurobiology, models and cognition. *Progress in neurobiology*, 158:132–152, 2017.

[79] John M Beggs and Dietmar Plenz. Neuronal avalanches in neocortical circuits. *Journal of neuroscience*, 23(35):11167–11177, 2003.

[80] John M Beggs and Nicholas Timme. Being critical of criticality in the brain. *Frontiers in physiology*, 3:163, 2012.

[81] Viktor K Jirsa, R Friedrich, Hermann Haken, and JA Scott Kelso. A theoretical model of phase transitions in the human brain. *Biological cybernetics*, 71(1):27–35, 1994.

[82] JAS Kelso, SL Bressler, S Buchanan, GC DeGuzman, MAFAH Ding, A Fuchs, and T Holroyd. A phase transition in human brain and behavior. *Physics Letters A*, 169(3):134–144, 1992.

[83] Stephen Coombes and John R Terry. The dynamics of neurological disease: integrating computational, experimental and clinical neuroscience. *European Journal of Neuroscience*, 36(2):2118–2120, 2012.

[84] Ben J Harrison, Murat Yücel, Jesus Pujol, and Christos Pantelis. Task-induced deactivation of midline cortical regions in schizophrenia assessed with fmri. *Schizophrenia research*, 91(1-3):82–86, 2007.

[85] Andreas Meyer-Lindenberg, Jean-Baptiste Poline, Philip D Kohn, John L Holt, Michael F Egan, Daniel R Weinberger, and Karen Faith Berman. Evidence for abnormal cortical functional connectivity during working memory in schizophrenia. *American Journal of Psychiatry*, 158(11):1809–1817, 2001.

[86] Ayna B Nejad, Bjørn H Ebdrup, Hartwig R Siebner, Hans Rasmussen, Bodil Aggernæs, Birte Y Glenthøj, and William FC Baaré. Impaired temporoparietal deactivation with working memory load in antipsychotic-naive patients with first-episode schizophrenia. *The World Journal of Biological Psychiatry*, 12(4):271–281, 2011.

[87] Susan Whitfield-Gabrieli, Heidi W Thermenos, Snezana Milanovic, Ming T Tsuang, Stephen V Faraone, Robert W McCarley, Martha E Shenton, Alan I Green, Alfonso Nieto-Castanon, Peter LaViolette, et al. Hyperactivity and hyperconnectivity of the default network in schizophrenia and in first-degree relatives of persons with schizophrenia. *Proceedings of the National Academy of Sciences*, 106(4):1279–1284, 2009.

[88] Joanes Grandjean. A common mouse fmri resource through unified preprocessing, 2020.

[89] Francesca Mandino, Yeow Ling Yun, John Gigg, Malini C. Olivo, and Joanes Grandjean. Mouse rest 3 x TG, 2019.

[90] Michael Schirner, Anthony Randal McIntosh, Viktor Jirsa, Gustavo Deco, and Petra Ritter. Inferring multi-scale neural mechanisms with brain network modelling. *Elife*, 7:e28927, 2018.

[91] Rahul S. Desikan, Florent Ségonne, Bruce Fischl, Brian T. Quinn, Bradford C. Dickerson, Deborah Blacker, Randy L. Buckner, Anders M. Dale, R. Paul Maguire, Bradley T. Hyman, Marilyn S. Albert, and Ronald J. Killiany. An automated labeling system for subdividing the human cerebral cortex on MRI scans into gyral based regions of interest. *NeuroImage*, 31(3):968–980, July 2006.

[92] Michael Schirner, Simon Rothmeier, Viktor K Jirsa, Anthony Randal McIntosh, and Petra Ritter. An automated pipeline for constructing personalized virtual brains from multimodal neuroimaging data. *NeuroImage*, 117:343–357, 2015.

[93] Edward Ott and Thomas M Antonsen. Low dimensional behavior of large systems of globally coupled oscillators. *Chaos: An Interdisciplinary Journal of Nonlinear Science*, 18(3):037113, 2008.

[94] Dean Prichard and James Theiler. Generating surrogate data for time series with several simultaneously measured variables. *Physical review letters*, 73(7):951, 1994.

[95] Daniel August Gehrlach, Thomas N Gaitanos, Alexandra S Klein, Caroline Weiand, Alexandru A Hennrich, Karl-Klaus Conzelmann, and Nadine Gogolla. A whole-brain connectivity map of mouse insular cortex. *BioRxiv*, 2020.

5 Figures and figure captions

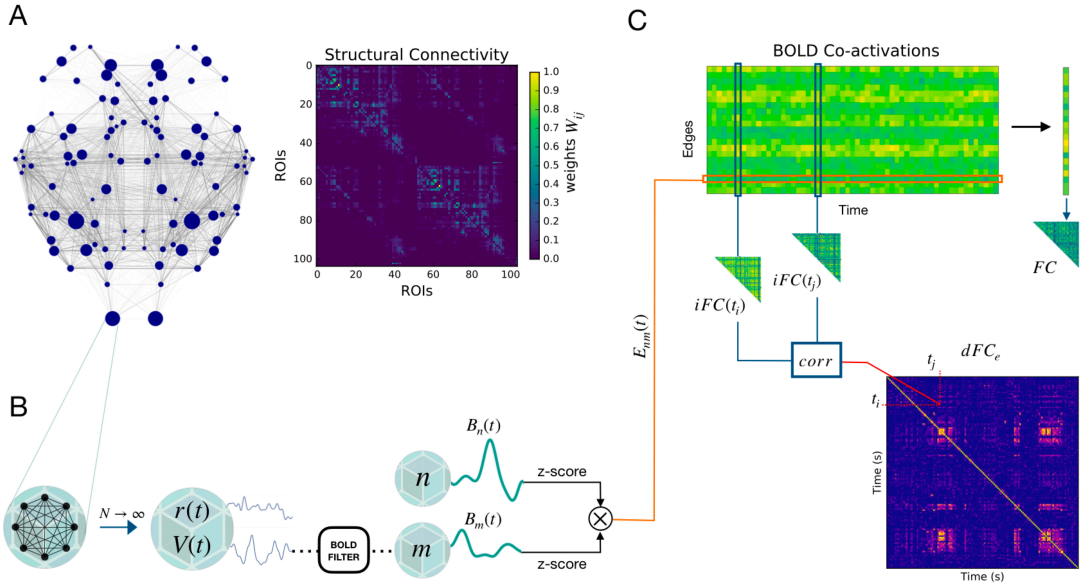

Figure 1: Connectome based modeling . (A) The mouse connectome imported from the tracer experiments of the Allen Institute. The 104 cortical regions of interest (ROIs) are specified in the table in Figure S4A. (B) The Neural Mass Model (NMM) used is derived as the thermodynamic limit of infinite quadratic integrate-and-fire (QIF) neurons. The outcome of the numerical integration of the NMM over the mouse connectome are neuroelectric time series for the average firing rate $r_n(t)$ and the average membrane potential $V_n(t)$ for each brain region. Applying the Balloon-Windkessel model to $V_n(t)$ we obtain the simulated BOLD signal $B_n(t)$. Given two nodes n and m the edge co-activation (CA) signal $E_{nm}(t)$ is defined as the product of the z-scored BOLD signal $B_n(t)$ and $B_m(t)$. (C) Each column of the BOLD-CA matrix represents and instantaneous realization of the Functional Connectivity (iFC). Averaging the $iFC(t)$ over time we obtain the static Functional Connectivity (FC). The elements (i, j) of the edge- dynamic Functional Connectivity (dFC_e) matrix are defined as the Pearson Correlation between $iFC(t_i)$ and $iFC(t_j)$.

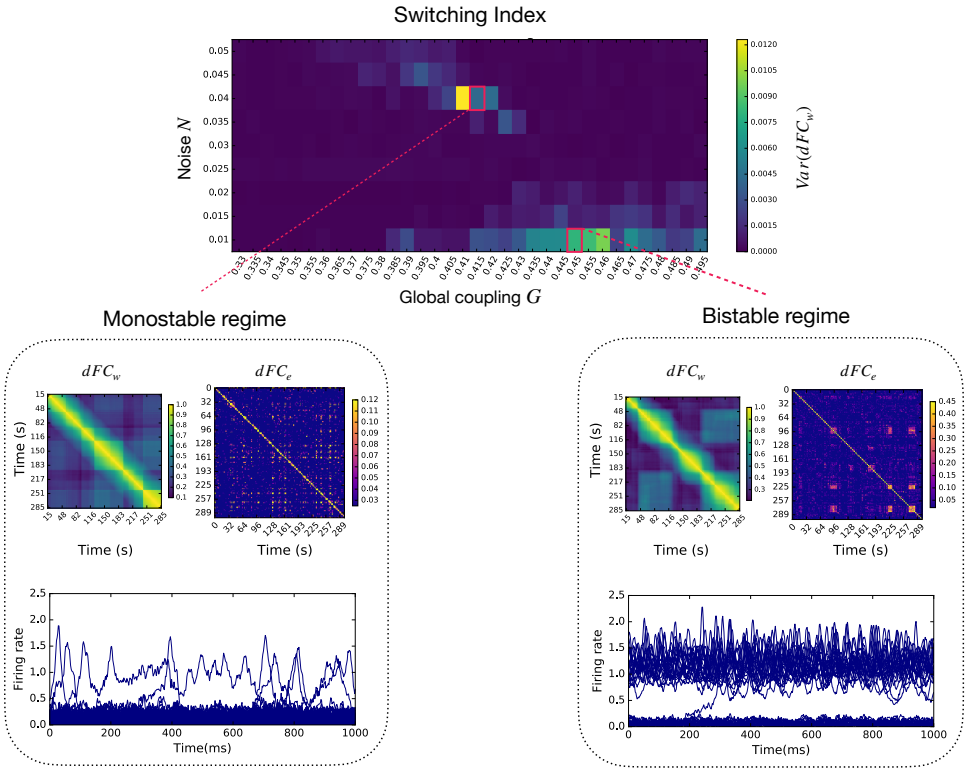

Figure 2: Two qualitatively distinct regimes of non-trivial functional dynamics. For every couple of global parameters (G, N) we calculated the dynamic functional connectivity (dFC) in a sliding window approach (dFC_w; as in Figure S1) and in an edge-centric approach (dFC_e; as shown in Figure 1C). The 'switching index' of each dFC_w matrix, was evaluated as the variance of the respective upper triangular part. We find two regimes of activity, named *monostable* and *bistable*, where qualitatively distinct neuroelectric organizations give rise to a large-scale functional dynamics characterized by a non-vanishing switching index. In the monostable regime, the dFC_w and dFC_e display off-diagonal blocks, demonstrating a correlation between the functional activity at distinct times. The low global coupling G in the monostable regime does not guarantee a strong communication between the brain network regions, which most of the time populate the low firing rate ('down') state. A strong noise N pushes the brain regions in the high firing rate ("up") state for short transients. Also in the bistable regime, the dFC_w and dFC_e display off-diagonal blocks. A higher value of the global coupling promotes a subgroup of regions in the high firing rate ('up') state. Low levels of noise perturb the equilibrium of the system provoking localized switching in both up→down and down→up directions.

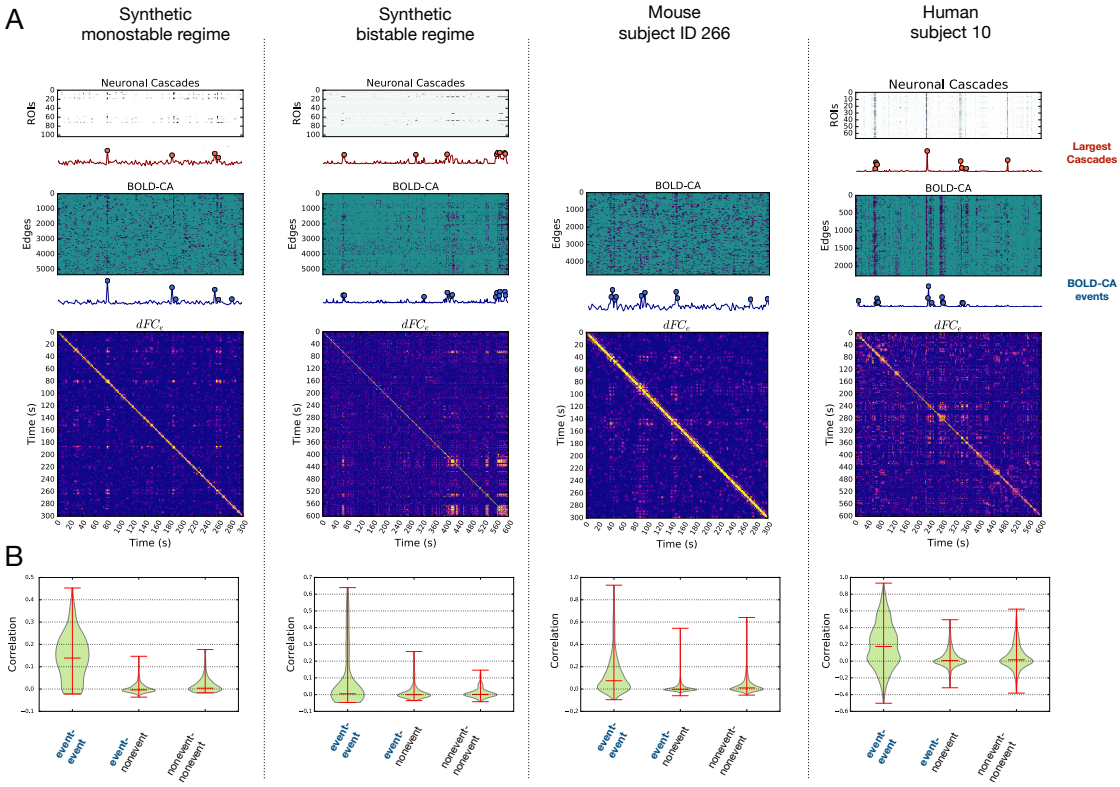

Figure 3: Neuronal cascades drive the functional dynamics. (A; top panels) Examples raster plots of the firing rate deviations from baseline activity in the monostable and bistable synthetic regime and for an example subject of the empiric EEG/fMRI Human dataset. In order to define the raster plot, a unitary value is assigned when a region goes above 3 standard deviations from its baseline activity, zero otherwise. Then, the binary sequence is reduced to the same resolution of the BOLD activity by averaging in non-overlapping time windows of 2 seconds (BOLD repetition time). This defines a sequence of *neuronal cascades*. The mean of the raster plot over the ROIs (red line) defines the cascade magnitude and shows the presence of large neuronal events (marked as red dots when above the 98th percentile). (A; middle panels) The BOLD-CA pattern in simulated and empiric mice and human datasets is also characterized by sudden collective events involving large network parts. Its root sum square (RSS, blue line) defines the collective edge CA amplitude. The largest BOLD-CA *events* (marked as blue dots above the 98th percentile of the RSS) are distinguished them from the *non-events* (below threshold). (A; bottom panels) The dFC_e matrices display non-trivial off-diagonal blocks. At a visual inspection, the BOLD-CA events seem to happen in coincidence with dFC_e blocks. In panel (B) we report the synthetic and empiric correlations between iFCs at times within CA events, between events and non-events, within non-events. These correlations are by definition the off-diagonal values of the dFC_e matrix. The distribution of the correlations within events is wider and explains the greatest off-diagonal correlation values of the dFC_e across all the synthetic and empiric datasets.

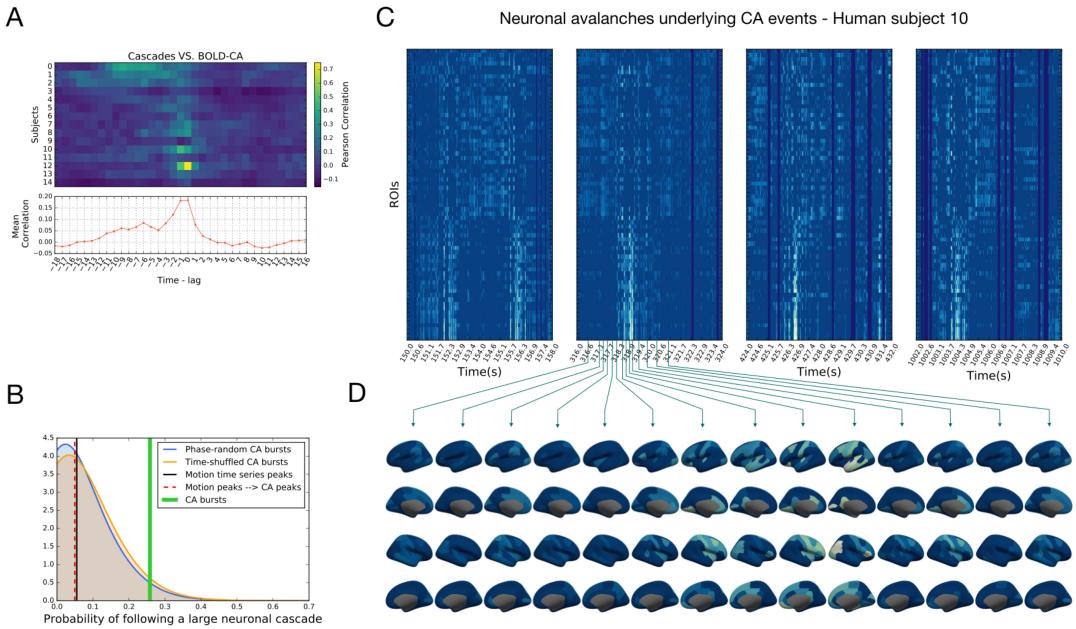

Figure 4: In both empiric and simulated data sets, the largest neuronal cascades seem to precede in most instance the BOLD-CA events (see Figure 3A). (A) We quantify this correspondence in the Human EEG/fMRI datasets by evaluating the correlation between the cascade magnitude and the BOLD-CA amplitude (red and blue lines in Figure 3A) for different subjects and different time lags. Negative lag is associated with a shift backward of the BOLD signal. (A; bottom) The peaks of correlation at lags 0 and -1, as well as the rapid fall for positive lags, confirms that the EEG precedes the BOLD activity by few seconds. (B) For the entire Human cohort we show the average probability (green line) to observe a large BOLD-CA event within few $(0-4)$ seconds after a large cascade (large events defined above the 98th percentile). The same probability is evaluated by comparing the largest cascades with the BOLD-CA events extracted from 100 time-shuffled (in orange) and 100 phase-randomized (cross-spectrum preserved, in blue) BOLD surrogates for every subject. The motion artifacts were eliminated in the BOLD data preprocessing. To double check our results we also compared the probability that a peak of the motion time series follows a large neuronal cascade (black line) and the probability that a BOLD-CA follows a peak of the head movement (dashed red). (C) High time resolution example of large neuronal cascades subtending a BOLD-CA in the empiric human dataset. The selected subject is the same as in Figure 3. Here we represent the cascades by z-scoring the EEG signal in every region and setting to zero the activity below 1 standard deviation. Each selected time interval corresponds to 8 seconds of activity in which at least one burst of BOLD CA is found. We notice that, at distinct times, a special group of regions gets consistently activated during the spread of the cascade. (D) Brain maps showing the propagation of the cascade in one time window.

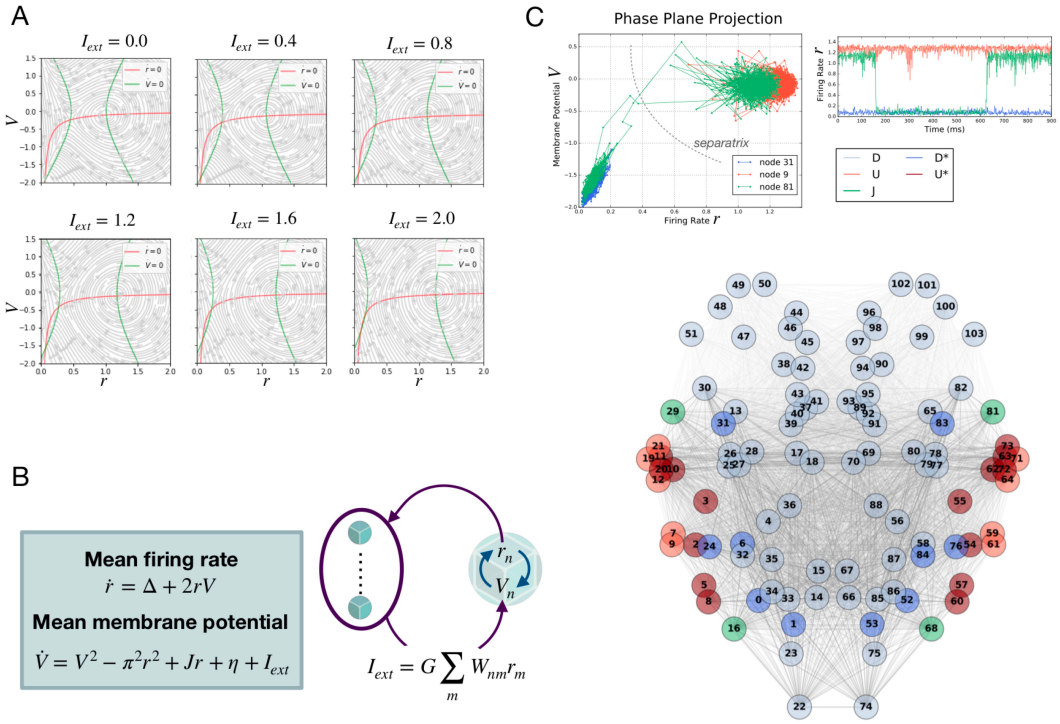

Figure 5: Mechanisms of cascade generation in the bistable synthetic model. (A) Phase Plane distortion: the phase plane of each decoupled node ($I_{ext} = 0$) has a down fixed point and a up stable focus. As the external current I_{ext} is increased, the phase plane of the neural mass changes, according to the equations in panel (B) (see also Methods). In particular, the basin of attraction of the up state gradually becomes larger than that of the down state, while the fixed points move farther apart. (B) From the local node perspective, the network action can be thought of as an input current which provokes a distortion of the phase plane. In fact, the firing rate of the coupled regions act as an excitatory external current I_{ext} in the local neural mass equations. Therefore, strongly connected regions within the network will have a higher probability of being attracted into the up state with a large basin of attraction. (C) Depending on the local distortion of the phase plane, different regions have a different fate. If the overall input is too low a region is confined into the down fixed point explored by noisy fluctuations (class D, light blue). If the input is too strong, a region remains stuck in the up stable focus plus noisy fluctuations (class U, light red). Only a subset of regions with the right level of input are capable of jumping over the separatrix between the up and down states. Few regions jump all the time throughout the simulation (class J, green). The dark red (class U*) and dark blue (class D*) regions dwell most of the time in the up and down states, respectively. Only in important rare occasions they cross the threshold to jump on the other side. (C, top left) Example of exploration of the projected 2D phase spaces by the 'up', 'down' and 'jumping' regions. (C, top right) Example time series of the firing rate in the three cases represented in the phase planes. (C, bottom) the spatial distribution of the (D, U, J, D*, U*) classes is extremely symmetric and shows a clear role of the structure in defining the local dynamics. In general, referring to Figure S4A, light blue regions include default network regions (anterior cingulate, retrosplenial, and hippocampus) but also cerebellum and some visual areas. Light red regions are temporal/lateral regions. Dark blue regions mainly include motor regions, but also the subiculum and the piriform. Dark red regions are mainly somatosensory. Green regions are the insula and entorhinal cortex, which are known to be connected [95]. The specific classification also depends on the chosen working regime and might change for different parameter configurations.

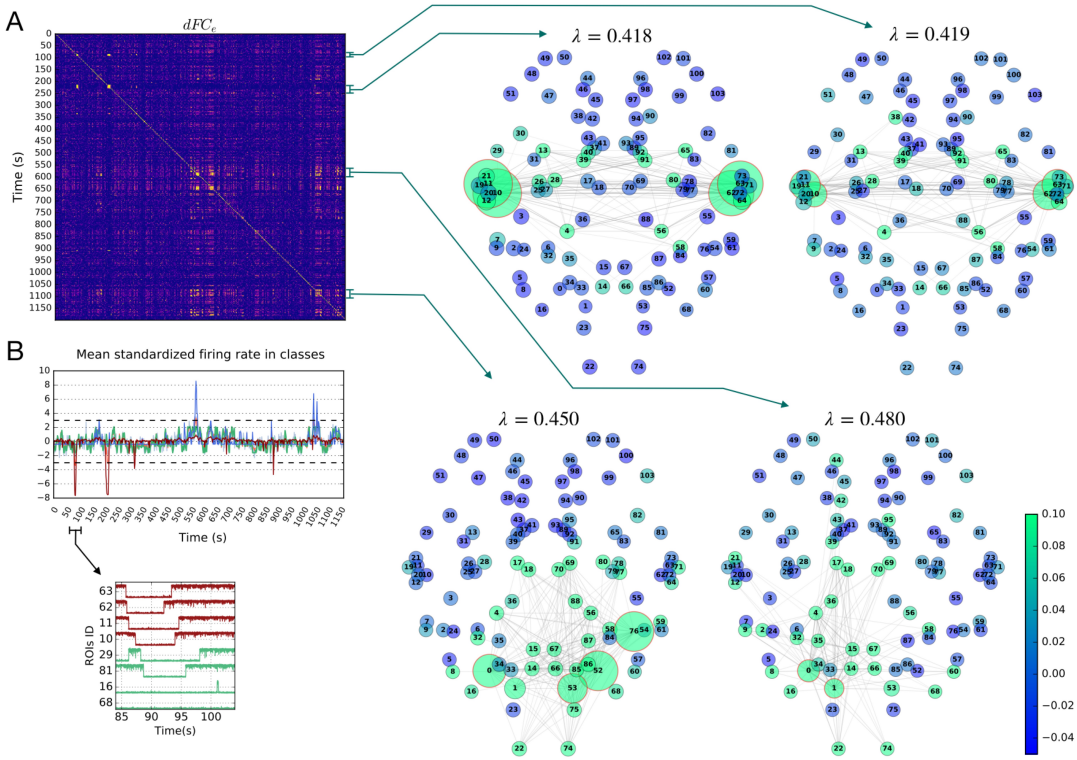

Figure 6: Cascades versus dynamic functional connectivity in the bistable regime. (A) Edge dynamic functional connectivity. (B, top) Average firing rate in the (U), (D), (J), (U*) and (D*) classes (z-scored). The dark red (U*) and dark blue (D*) classes exceed the threshold (dashed lines) and carry other regions of the network away from baseline for a short transient. (B, bottom) Example of avalanche: when the node 63 jumps into the down state, it first drags down the node 62 (with which it shares the strongest structural link in the network). After them, other strongly connected nodes follow the trend. Therefore, the rare events happening at the 'star' regions elicit the largest neuronal avalanches in the brain. As we discussed, each avalanche elicits a specific BOLD-CA event which emerges as a stable functional state (diagonal block in the dFC_e). The same avalanche occurring in succession elicit the same functional state (off-diagonal block in the dFC_e). On the right, we show some example functional networks associated to dFC_e blocks. Each network is defined as the leading eigenvector (eigenvalue λ) of the iFC matrix at times corresponding to the dFC_e blocks (see Figure 1C). The two functional networks on the top are elicited by (U*) jumps and are dominated by cortical sensory regions. The two networks on the bottom are generated from (D*) jumps and involve high-order control regions (motor, cingulate, retrosplenial). We draw the edges carrying the strongest BOLD co-activation. The radius of the network nodes is higher depending on the participation of a node into the neuronal cascade subtending the functional network.